Facile synthesis of sulfate-doped Ag$_3$PO$_4$ with enhanced visible light photocatalystic activity

Wenrong Cao, Zhenyou Gui, Lifang Chen*, Xuedong Zhu, Zhiwen Qi

State Key Laboratory of Chemical Engineering, School of Chemical Engineering, East China University of Science and Technology, Shanghai 200237, China

A B S T R A C T

Sulfate-doped Ag$_3$PO$_4$ photocatalysts were successfully synthesized via a simple precipitation method. The X-ray diffraction (XRD) and X-ray photoelectron spectroscopy (XPS) confirmed that SO$_4^{2-}$ ions were incorporated into the lattice of Ag$_3$PO$_4$ by replacing PO$_4^{3-}$. The crystalline structure and optical absorption behavior of Ag$_3$PO$_4$ remain unchanged after SO$_4^{2-}$ doping. However, SO$_4^{2-}$-doped Ag$_3$PO$_4$ catalyst with 0.50 at% SO$_4^{2-}$ concentration ratio exhibited remarkably enhanced photocatalytic activity, and completely decomposed rhodamine B (RhB) and methylene blue (MB) in 4 and 5 min under visible light irradiation, respectively. Its degradation rate constant was more than 5 times higher than that of pristine Ag$_3$PO$_4$. The high photocatalytic performance is attributed to the fact that doping SO$_4^{2-}$ into Ag$_3$PO$_4$ lattice can improve the separation efficiency of photogenerated electron-hole pairs and hinder their recombination. In addition, the results of density functional theory (DFT) calculations indicate that SO$_4^{2-}$ substitution can effectively tune the electronic structures of Ag$_3$PO$_4$, thus resulting in high photocatalytic activity under visible light irradiation.

© 2016 Elsevier B.V. All rights reserved.

1. Introduction

Nowadays, semiconductor photocatalysts have been widely applied in environment remediation and energy shortage because they can directly harvest the incoming solar energy [1–3]. Among numerous semiconductor materials, TiO$_2$ is considered as an efficient photocatalyst to mineralize organic pollutants owing to its photostability, non-toxicity and low cost [4–6]. However, TiO$_2$ suffers from the inferior utilization of visible light because of its wide band gap energy, which restricts its practical applications [7]. Therefore, it is of great importance and necessity to explore highly efficient visible-light-responsive photocatalysts for application in environmental pollution remediation.

Recently, silver orthophosphate (Ag$_3$PO$_4$) has been reported as an efficient photocatalytic material for water photooxidative and organic dye degradation under visible light irradiation [8,9]. However, pristine Ag$_3$PO$_4$ still encounters low-efficient charge-transport characteristics, resulting in low photocatalytic activity. To solve this problem, numerous attempts have been made to improve the photocatalytic performance of Ag$_3$PO$_4$, mainly including the morphological modulation and heterojunctions fabrication

[10,11]. For example, Ag$_3$PO$_4$ rhombic dodecahedrons with high energy {110} facets exhibited much higher photocatalytic activities than cubes with low energy {100} facets and irregular particles for the degradation of organic contaminants [9]. In addition, the coupling of Ag$_3$PO$_4$ with other semiconductors, such as AgX/Ag$_3$PO$_4$ (X = Cl, Br, I), Ag$_3$PO$_4$/TiO$_2$, Ag$_3$PO$_4$/SnO$_2$, graphene oxide/Ag$_3$PO$_4$, MoS$_2$/Ag$_3$PO$_4$, etc. have enhanced photocatalytic activity and stability as compared to pure Ag$_3$PO$_4$ [12–16].

Doping suitable cations or anions into the lattice of a photocatalyst is another feasible approach to modulate the band gap structure, and consequently improves its photocatalytic performance [17–19]. To date, doping suitable cations (Bi^{3+}, La^{3+}, Ba^{2+} et al.) into Ag$_3$PO$_4$ lattice has been reported to enhance photocatalytic performance of Ag$_3$PO$_4$ [20–22]. Among cation dopants, Bi^{3+} inserted into P^{5+} sites of the host Ag$_3$PO$_4$ lattice could reduce OH defects and influence the electronic structure of Ag$_3$PO$_4$, which shows relatively high photocatalytic performance. However, it is rarely investigated to achieve suitable anions doping into Ag$_3$PO$_4$ lattice with superior photocatalytic performance.

Noticeably, it has recently been demonstrated that doping sulfur into phosphorous sites in the host lattice of Ag$_3$PO$_4$ can yield high carrier concentration and control electrical properties on the basis of hybrid density-functional calculations [23]. Thereby, doped Ag$_3$PO$_4$ with sulfur can offer opportunities to improve the photocatalytic activity of Ag$_3$PO$_4$. However, incorporating sulfur into

---

the lattice of Ag_3PO_4 is very difficult through post-treated process owing to the strong P-O bond. It should cost much energy to inset those dopant into PO_4 matrix. Additionally, oxoanion groups, such as PO_4^{3-} and CO_3^{2-}, have been used as dopant for semiconductor photocatalysts, which can modulate the crystal structure, optical properties, electronic structure of semiconductor materials and consequently enhance the photocatalytic activity [24,25]. Therefore, SO_4^{2-} could be one of the potential doping ions for Ag_3PO_4, since SO_4^{2-} has the similar ion radii with PO_4^{3-} [26].

Herein, we experimentally synthesized SO_4^{2-}-doped Ag_3PO_4 by replacing some of PO_4^{3-} in the lattice of Ag_3PO_4 using a simple precipitation method. Sodium sulfate as sulfate source plays a critical role in the formation of SO_4^{2-}-doped Ag_3PO_4. In comparison with pure Ag_3PO_4, SO_4^{2-}-doped Ag_3PO_4 catalysts exhibited superior photocatalytic performance for the degradation of rhodamine B (RhB) and methylene blue (MB) under visible light irradiation. Moreover, the enhanced photocatalytic performance was investigated by spectral characterizations, photoelectrochemical measurements and density functional theory (DFT) calculations.

2. Experimental

2.1. Catalyst preparation

All reagents were of analytical grade and used without further purification. In a typical procedure, 0.2 g $AgNO_3$ was dissolved in 40 mL distilled water at room temperature. In order to obtain homogeneous SO_4^{2-} doped Ag_3PO_4 samples, different amounts of Na_2SO_4 (variable from 0, 0.28, 4.2, 83.6 mg to 1.672 g) were first added into the above solution to form a transparent solution under constant stirring for 15 min. Then the solution was added drop by drop into 20 mL Na_2HPO_4 aqueous solution (0.02 M) with continuous stirring. The obtained precipitate was collected by centrifugation, washed with distilled water and ethanol for several times, and dried at 60 °C for 6 h. The corresponding samples were denoted as AP-0, AP-1, AP-2, AP-3, and AP-4 respectively.

2.2. Characterization

The crystalline phases of the products were examined by power X-ray diffraction (XRD, Bruker D8 Advance diffractometer) with Cu-Kα radiation (Kα_1 = 1.5406 Å, Kα_2 = 1.5444 Å) in the range of $2\theta = 20-80°$. Kα_2 lines were simultaneously subtracted from the background correction of raw XRD data. The surface morphologies of the products were observed by field-emission scanning electron microscopy (FESEM, Nova NanoSEM 450). The energy-dispersive X-ray spectroscopy (EDS) mappings were presented on a FEI Tecnai G2 F20 S-Twin to determine the elemental distributions of the obtained products. The actual contents of sulfate in SO_4^{2-}-doped Ag_3PO_4 catalysts were determined by inductively coupled plasma-atomic emission spectroscopy (ICP-OES) on an Agilent 725ES instrument. The X-ray photoelectron spectroscopy (XPS) analyses were performed by a Thermo Scientific ESCALAB 250Xi X-ray photoelectron spectrometer with Al Kα X-ray as the excitation source. All binding energies were referred to the C 1s peak at 284.8 eV of the surface adventitious carbon. The Brunauer-Emmett-Teller (BET) specific surface areas of the samples were determined by nitrogen adsorption/desorption isotherms at liquid nitrogen temperature with Micromeritics ASAP 2010 instrument. The UV–vis diffuse reflectance spectra (DRS) were carried out on a Shimadzu UV-2450 spectrophotometer in the wavelength range of 200–800 nm, using $BaSO_4$ as background. The photoluminescence (PL) spectra were obtained on a Shimadzu RF-5301PC fluorescent spectrophotometer with an excitation wavelength of 325 nm.

2.3. Computational method

The theoretical calculations were performed using plane-wave pseudopotential DFT (+U) approach as implemented in the CASTEP code [27]. The local density approximation (LDA) was adopted as the exchange-correlation function. The ultrasoft pseudoptential was used to describe the interaction between the ionic core and valence electrons. To investigate the effect of SO_4^{2-} doping, the structures of SO_4^{2-}-doped Ag_3PO_4 were constructed on the basis of 288-atom $3 \times 3 \times 2$ supercell with one P replaced by S, 128-atom $2 \times 2 \times 2$ supercell with one or two P replaced by S, corresponding to 2.78 at%, 6.25 at% and 12.5 at% SO_4^{2-} concentration ratios, respectively. The kinetic cut-off energy for the plane wave expansion was set at 340 eV and the Monkhorst-Pack k-point mesh of $2 \times 2 \times 2$ was used. The on-site Coulomb repulsion (Hubbard U) was applied for Ag d, P p, O p and S p states, and U values were set to 7.2, 7.0, 7.0 and 7.0 eV, respectively. The geometry optimizations were necessary before running single-point energy calculation, and the convergence tolerance parameters of optimized calculations were energy of 1×10^{-5} eV/atom, a maximum force 0.03 eV/Å, a maximum stress of 0.05 GPa and a maximum displacement of 0.002 Å.

2.4. Electrochemical analyses

The electrochemical impedance spectroscopy (EIS) was performed by an Autolab PGSTAT 302 electrochemical workstation operating in a standard three-electrode cell at room temperature. The prepared sample, a platinum wire and a saturated calomel electrode were used as the working, counter and reference electrodes, respectively. The electrolyte was 0.5 M KNO_3 aqueous solution. EIS measurements were recorded in the open circuit potential mode with the frequency range of 50 mHz to 100 kHz under visible light irradiation. The visible light source was obtained from a 300 W Xe lamp with a 420 nm cut-off filter.

2.5. Photocatalytic activity test

The photocatalytic properties of as-prepared photocatalysts were evaluated by the degradation of RhB and MB under visible light irradiation. The visible light was obtained from a 350 W Xe lamp equipped with a 420 nm ultraviolet cutoff filter. The distance between the lamp and reactor was kept at a constant height of 15 cm. In a typical photocatalytic experiment, 20 mg of photocatalyst was added into 100 mL of 5 mg/L RhB or MB aqueous solution and then ultrasonicated for 10 min. The suspensions were magnetically stirred for 30 min in the dark to reach an adsorption-desorption equilibrium between photocatalysts and dye molecules prior to irradiation. During irradiation, 4 mL of suspensions were taken out at regular time intervals and centrifuged to remove the photocatalyst. The residual concentrations of RhB and MB were analyzed with a PerkinElmer Lamda 35 UV–vis spectrophotometer.

To investigate the photocatalytic stability of the prepared catalysts, the recycle experiments of RhB degradation over AP-3 catalyst were performed under visible light irradiation. For comparison, the experiment conditions are the same with the reported Bi^{3+}-doped Ag_3PO_4, which can significantly enhance the photocatalytic activity of Ag_3PO_4 compared with other dopants (La^{3+}, Ba^{2+}) [20–22]. Typically, the visible light source was a 300 W xenon lamp with a 420 nm cutoff filter, the amount of AP-3 catalyst was 100 mg and the targeted pollutant was 100 mL of 10 mg/L RhB aqueous solution. After each catalytic cycle, the catalyst was recovered by centrifugation, thoroughly washed with distilled water and ethanol for several times, and dried at 60 °C for 6 h. Then the recovered catalyst was reused in the subsequent run under the same conditions.
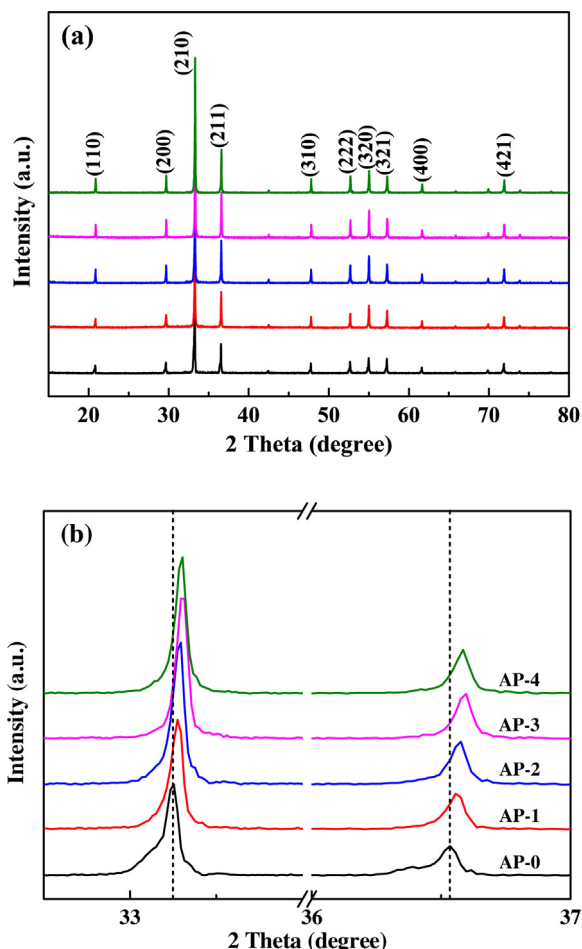
Fig. 1. (a) X-ray diffraction patterns of AP-0, AP-1, AP-2, AP-3 and AP-4 catalysts; (b) magnified peaks of (210) and (211) planes.

3. Results and discussion

3.1. Photocatalyst characterization

The XRD patterns were performed to investigate the effect of SO_4^{2-} doping on the crystal structure of Ag_3PO_4, as shown in Fig. 1. All diffraction peaks of the samples can be well indexed to the body-centered cubic structure of Ag_3PO_4 (JCPDS No. 06-0505). No impurity phase such as Ag_2SO_4 and Ag observed in SO_4^{2-}-doped Ag_3PO_4 implies that SO_4^{2-} doping does not affect the crystal structure of Ag_3PO_4. Fig. 1b exhibits the magnified XRD patterns of (210) and (211) peaks, which show gradual shifts of peaks toward higher angles with increasing dopant concentration. The calculated lattice constants for AP-0, AP-1, AP-2 and AP-3 catalysts are 6.019, 6.015, 6.013 and 6.009 Å, respectively. Doping SO_4^{2-} into Ag_3PO_4 causes a decrease in the lattice constants, since the ionic radius of SO_4^{2-} (0.218 nm) is less than that of PO_4^{3-} (0.230 nm) [26,28]. When the amount of Na_2SO_4 is further increased, the peaks positions and lattice constant of AP-4 catalyst exhibit almost the same as those of AP-3, indicating that no more SO_4^{2-} could substitute PO_4^{3-}. Herein, the XRD results confirm that replacing PO_4^{3-} by SO_4^{2-} is feasible to form SO_4^{2-}-doped Ag_3PO_4 experimentally.

To investigate the surface valence state and chemical composition of the samples, the XPS analyses of AP-0 and AP-3 catalysts were performed. Fig. 2 shows the high-resolution XPS spectra of S 2p, Ag 3d, P 2p and O 1 s of AP-0 and AP-3 samples, respectively. Fig. 2a shows the peak at around 168.40 eV associated with S 2p in AP-3 catalyst is assigned to S^{6+} [29], which confirms that SO_4^{2-} may

be incorporated into the Ag_3PO_4 lattice. In Fig. 2b, the Ag 3d spectra of AP-0 and AP-3 samples consist of two major peaks around 367.53 and 373.53 eV, 367.70 and 373.70 eV, corresponding to the Ag $3d_{5/2}$ and Ag $3d_{3/2}$ binding energies of Ag^+ species, respectively [30]. The observed P 2p peaks appear at 132.40 eV for AP-0 and 132.60 eV for AP-3 sample in Fig. 2c, which can be assigned to the binding energy of P^{5+} in Ag_3PO_4. Therefore, SO_4^{2-} doping has negligible effect on the chemical valence states of Ag and P elements. Moreover, the binding energies of both Ag 3d and P 2p peaks of AP-3 sample increase to higher values compared with those of AP-0. Such behavior suggests that doping SO_4^{2-} can decrease the electron densities around Ag and P due to the higher electronegativity of S than P atom [31]. The similar results also occur for the binding energies of O 1 s (Fig. 2d). The binding energy of O 1 s for AP-3 sample increases by about 0.13 eV as compared to AP-0 sample. The XPS analyses indicate that the existence of S in the form of SO_4^{2-} in Ag_3PO_4 crystal lattice has strong electronic interactions with Ag, P, and O elements [20].

The detailed morphologies of pristine and SO_4^{2-}-doped Ag_3PO_4 were observed by FESEM. Fig. 3a shows the irregular particles of AP-0 catalyst with diameters ranging from 200 to 400 nm. The morphologies and sizes of AP-1 and AP-3 samples (Fig. 3b and c) almost remain unchanged due to a small amount of SO_4^{2-} incorporated into the lattice of Ag_3PO_4 during the preparation. However, a mixture of polyhedral and irregular particles are presented in AP-4 sample with further increasing the amount of SO_4^{2-}, and the particle sizes evidently increase with diameters ranging from 400 to 750 nm. This can signify that a far excessive concentration of inorganic SO_4^{2-} from Na_2SO_4 may be as a surfactant adsorbed on the surface of Ag_3PO_4 crystal nuclei, thereby influencing the formation of particles morphologies [32].

In order to demonstrate the existence of SO_4^{2-} in AP-3 catalyst, TEM EDS elemental mapping was investigated in Fig. 4. The results show that Ag, P, O and S elements are relatively homogeneous distributions within the AP-3 catalyst. Thus, EDS, XRD and XPS results confirm that SO_4^{2-} has been successfully doped into the Ag_3PO_4 lattice. In addition, the actual contents of sulfur in SO_4^{2-}-doped Ag_3PO_4 samples were also analyzed by ICP-AES. The atomic ratios of SO_4^{2-} to PO_4^{3-} in AP-1, AP-2, AP-3 and AP-4 samples are about 0.07 at%, 0.14 at%, 0.50 at% and 0.53 at%, respectively. The contents of SO_4^{2-} are much less than initial amounts of Na_2SO_4 introduced during the preparation. It indicates that the doping of SO_4^2 into Ag_3PO_4 lattice is very difficult and excess amount of SO_4^{2-} in the preparation is essential for the doping process.

3.2. Photototcatalytic activity

The photocatalytic activities of pure Ag_3PO_4 and SO_4^{2-}-doped Ag_3PO_4 catalysts were evaluated by the degradation of RhB and MB under visible light irradiation. Fig. 5 shows the degradation curves of RhB and MB over different catalysts. The blank experiments demonstrate that the degradation of RhB and MB solution is negligible in the absence of photocatalyst, indicating that the self-photolysis of RhB and MB can be ignored.

As shown in Fig. 5a, AP-0 catalyst shows relatively weak activity, and can completely degrade RhB within 20 min irradiation. Apparently, SO_4^{2-}-doped Ag_3PO_4 catalysts exhibit much higher photocatalytic activities than pure Ag_3PO_4. Moreover, an interesting observation is that AP-3 sample shows the best photocatalytic performance and can completely decompose RhB in only 4 min. AP-1, AP-2 and AP-4 catalysts can decompose RhB dye in 10, 8 and 8 min, respectively. Additionally, the photocatalytic performances of as-prepared catalysts for the MB degradation under the same conditions are also shown in Fig. 5b. The photoreactivity order of these catalysts is highly consistent with the above results for RhB degradation.
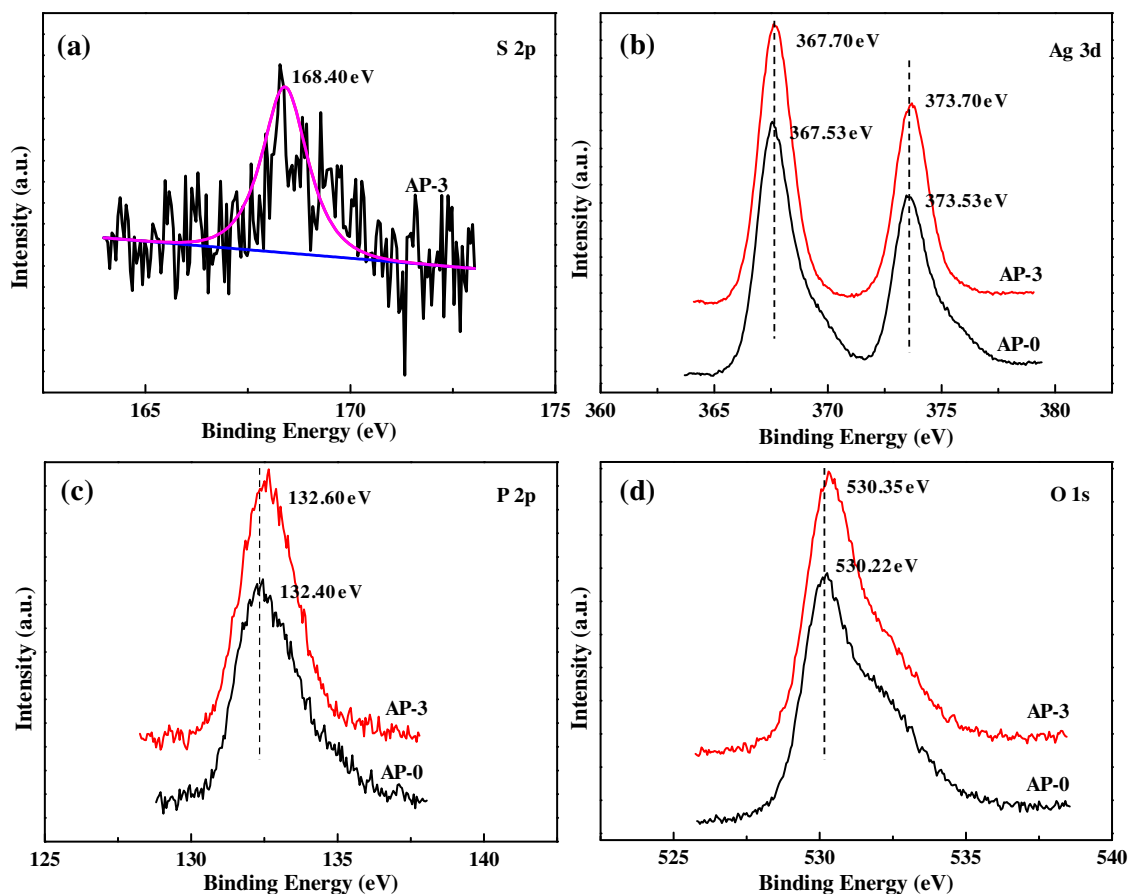
Fig. 2. High-resolution XPS spectra of AP-0 and AP-3 samples. (a) S 2p, (b) Ag 3d, (c) P 2p, (d) O 1s.
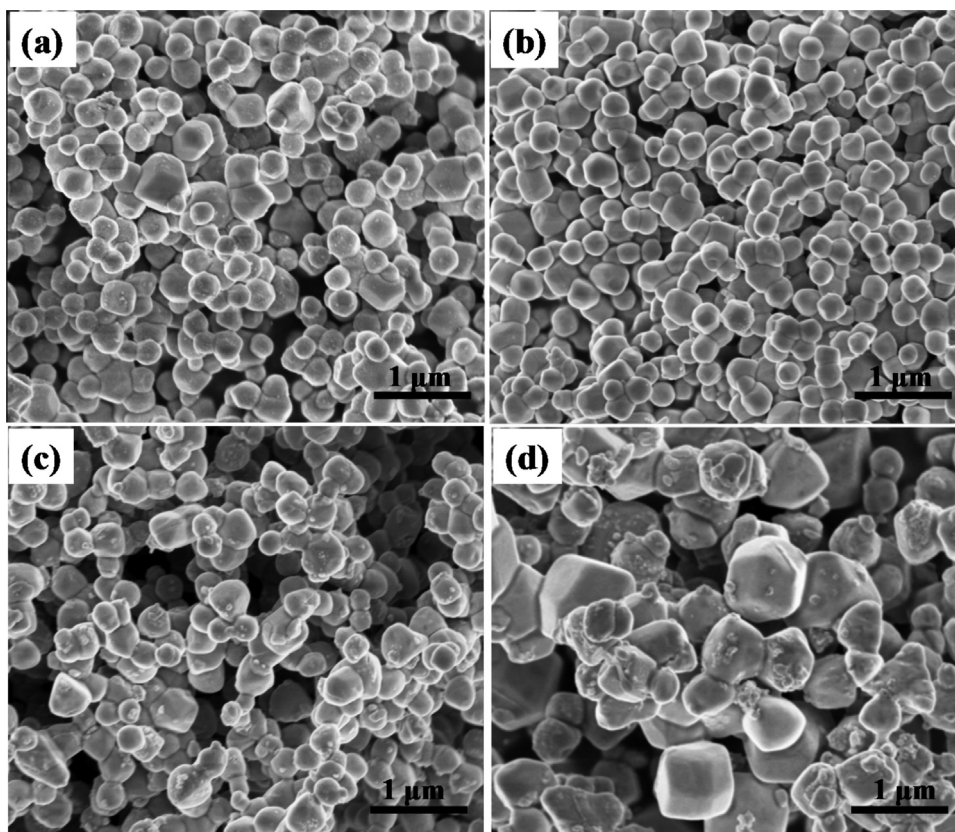

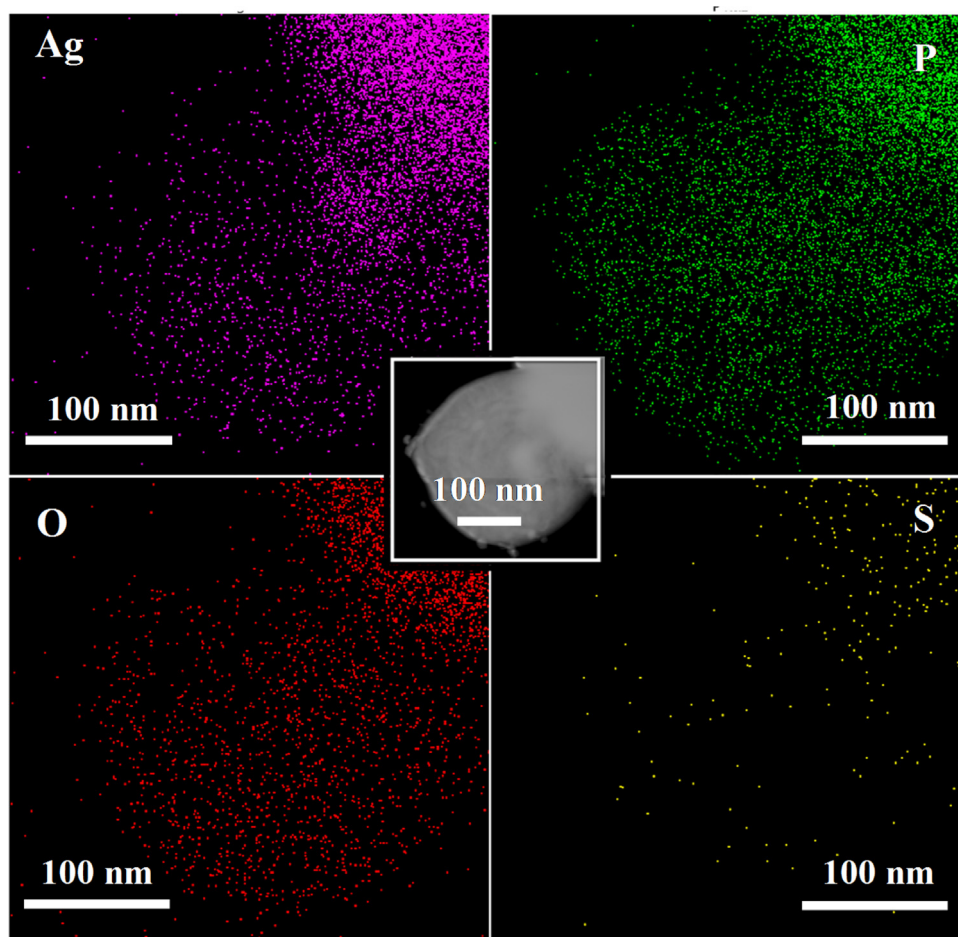**Fig. 3.** FESEM images of (a) AP-0, (b) AP-1, (c) AP-3 and (d) AP-4 samples.

Fig. 4. EDS mapping of Ag, P, O and S elements for AP-3 catalyst. The inset shows the corresponding TEM image for elemental mapping.

Table 1
Kinetic constants and regression coefficients of the degradation of RhB and MB catalyzed by pure Ag_3PO_4 and various doped samples.

Catalyst	RhB		MB	
	k (min^{-1})	R^2	k (min^{-1})	R^2
AP-0	0.1607	0.9996	01275	0.9961
AP-1	0.3553	0.9986	0.2947	0.9960
AP-2	0.4807	0.9979	0.4035	0.9942
AP-3	0.9002	0.9975	0.6895	0.9983
AP-4	0.4324	0.9999	0.3858	0.9990

To comprehend the photocatalytic reaction process, the photocatalytic degradation kinetics of RhB and MB were also performed in the present work. The linear relations of $\ln(C/C_0)$ versus the irradiation time are observed for all catalysts under visible light irradiation as shown in Fig. 6. The photocatalytic behavior accords with the Langmuir-Hinshelwood first-order reaction kinetics, which can be expressed in the following equation [33]:

$$\ln(C/C_0) = -k_{app}t \tag{1}$$

where k_{app} and t represent the apparent reaction rate constant and time, respectively. The rate constants (k_{app}) and regression coefficients (R^2) in the experiments are calculated and summarized in Table 1. In the degradation of RhB, AP-3 catalyst presents the highest rate constant (ca. 0.9002 min^{-1}), which is approximately 5.6 times as high as AP-0 (ca. 0.1607 min^{-1}), and the order of k values is found to be AP-3 > AP-2 > AP-4 > AP-1 > AP-0. For the degradation of MB, AP-3 sample still displays the best photocatalytic activity

and the rate constant of AP-3 is 5.4 times higher than that of AP-0 sample. Moreover, as the same with photoreactivity order, the law for the kinetic constants of all samples is similar with the above results for RhB degradation.

As a result, SO_4^{2-}-doped Ag_3PO_4 samples can display significantly enhanced photocatalytic performance compared with pure Ag_3PO_4. Moreover, the amount of SO_4^{2-} has an obvious effect on the photocatalytic activity of Ag_3PO_4. In our case, the optimal doping concentration ratio of SO_4^{2-} is 0.50 at% in AP-3 sample. When SO_4^{2-} doping content is below the optimal value, the photocatalytic activity could be enhanced with the increasing dopant concentration. The reason is that the dopant can trap and transfer electrons and holes to inhibit the recombination of electron-hole pairs [24]. However, when excess Na_2SO_4 is added, no more SO_4^{2-} could substitute PO_4^{3-}. The absorption of SO_4^{2-} on the surface of Ag_3PO_4 increase the particle sizes of AP-4 catalyst, which is detrimental to the photocatalytic activity. Therefore, an appropriate amount of Na_2SO_4 is crucial to optimize the SO_4^{2-} doping in Ag_3PO_4, thereby improving the photocatalytic activity.

Besides the excellent photocatalytic activity, the recyclability of the photocatalyst is crucially important for the practical application. The recycle experiments for RhB degradation over AP-3 catalyst were carried out under visible light irradiation. As shown in Fig. 7, it is found that AP-3 catalyst can completely decompose RhB within 4 min in the first cycle. The reaction rate constant is 0.9970 min^{-1}, which is 4.5 times higher than that of previously reported Bi^{3+}-Ag_3PO_4 (0.2207 min^{-1}) under the same experiment conditions [20]. It has a slight loss after two cycling runs, and subsequently maintains a stable photocatalytic perfor-
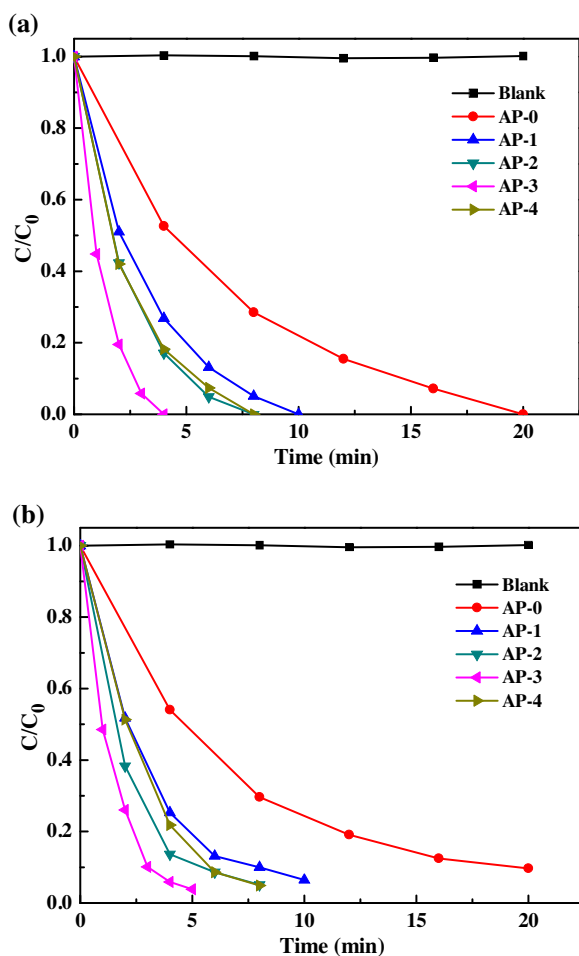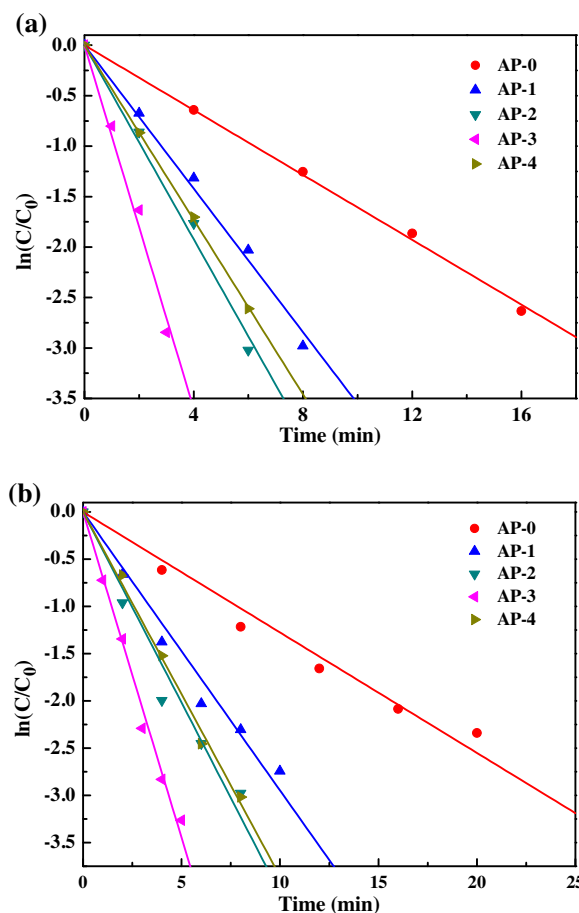
Fig. 5. Photodegradation of (a) RhB and (b) MB catalyzed by pure Ag_3PO_4 and various doped samples under visible light illumination.

Fig. 6. Kinetic linear simulation of (a) RhB and (b) MB photocatalytic degradation with pure Ag_3PO_4 and various doped samples.

mance. Specifically, the photodegradation efficiency of RhB still reaches about 98% in 5 min irradiation after six successive cycles, which is still much higher than that of Bi^{3+}-Ag_3PO_4 [20]. The slight decrease of photocatalytic activity could be mainly due to reduction of partial Ag^+ to metallic Ag^0 species in the initial reaction process. The formed $Ag@SO_4^{2-}$-Ag_3PO_4 plasmonic photocatalyst can still effectively maintain its activity because of the fast transfer of photoinduced electron-hole pairs [34,35].

3.3. Discussion for the improved photocatalytic activity of SO_4^{2-}-doped Ag_3PO_4

SO_4^{2-}-doped Ag_3PO_4 samples, especially AP-3, display excellent photocatalytic properties under visible light irradiation. Therefore, it is important to explore the relationship between the superior photocatalytic performance and surface (or structure) property. It is reported that the high BET surface area of catalysts could improve their photocatalytic performance [36]. However, Ag_3PO_4 and SO_4^{2-}-Ag_3PO_4 catalysts show similar and very small surface areas (1.8–2.5 m^2/g). It indicates that the specific surface areas of photocatalysts are not the main dominant factors on the photocatalytic activity. The significant differences in photocatalytic activities may be due to the doping of SO_4^{2-} into Ag_3PO_4 lattice. In order to further disclose the origin of the superior photocatalytic performance of SO_4^{2-}-doped Ag_3PO_4 catalysts, the relevant characterizations and DFT calculations were performed as follows.

The UV–vis diffuse reflectance spectra of pure Ag_3PO_4 and all SO_4^{2-}-doped Ag_3PO_4 were illustrated in Fig. 8a. All samples exhibit
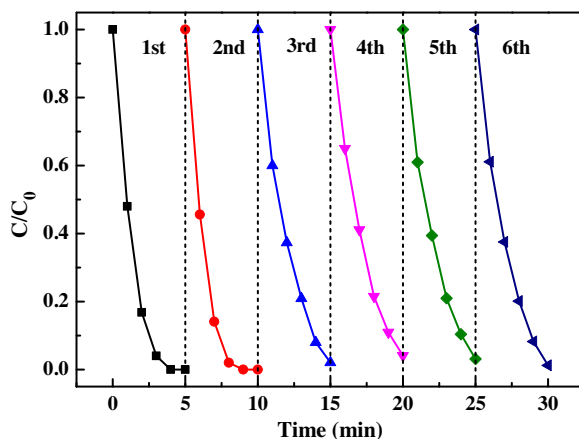

Fig. 7. Cycling runs for 10 mg/L RhB photodegradation over AP-3 catalyst under visible light irradiation. The concentration of AP-3 catalyst is 1.0 g/L and the visible light source is provided by a 300 W xenon lamp (λ > 420 nm).

almost identical absorption abilities in the visible light region. The optical band gap energies (E_g) of the samples are estimated by Mulliken electronegativity theory using the following formula [37]:

$$\alpha h\nu = A(h\nu - E_g)^{n/2} \tag{2}$$

where α, ν, A and E_g are the absorption coefficient, light frequency, absorption constant and band gap, respectively. The value of n depends on whether the transition is direct (n = 1) or indirect (n = 4). Since Ag_3PO_4 is an indirect band gap semiconductor, the value

(a)

(b)
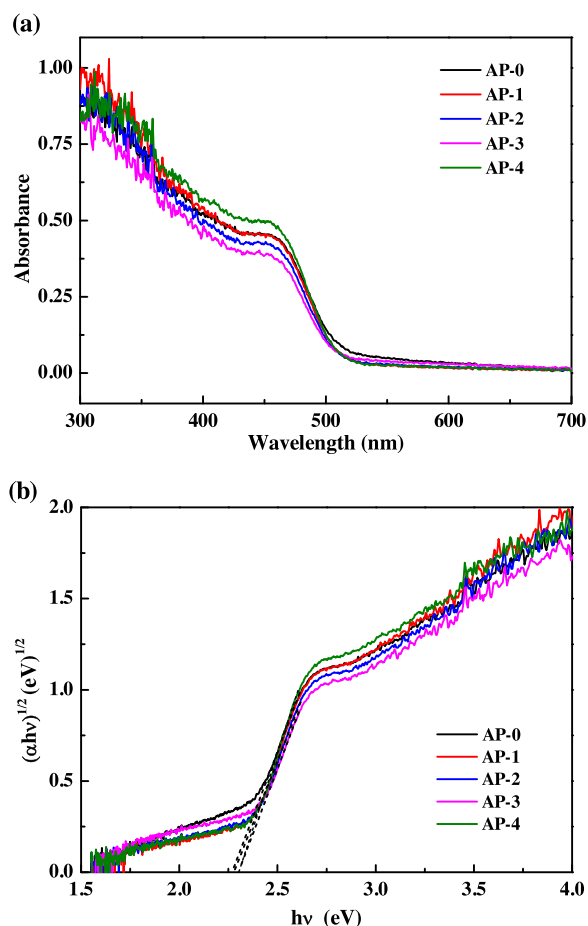

Fig. 8. (a) UV–vis diffuse reflectance spectra and (b) Plot of $(\alpha h\nu)^{1/2}$ versus energy $(h\nu)$ of as-prepared catalysts.

(a)

(b)

Fig. 9. (a) Room-temperature PL spectra of AP-0 and AP-3 catalysts under excitation at 325 nm, (b) EIS Nyquist plots of pure Ag_3PO_4 and all SO_4^{2-}-Ag_3PO_4 samples.

Fig. 10. Reactive species trapping experiments over AP-3 catalyst under visible light irradiation.

of n equals 4. Consequently, E_g can be estimated from a plot of $(\alpha h\nu)^{1/2}$ versus photon energy $(h\nu)$. The X-intercept of the tangent line gives an approximation of the band gap energy of the samples. As shown in Fig. 8b, the optical band gap energies of all samples are not much different. The band gap energy of AP-0 catalyst is 2.26 eV, and the band gap energies of SO_4^{2-}-doped Ag_3PO_4 are estimated to be 2.28–2.29 eV. It indicates that the band gap energies of SO_4^{2-}-doped Ag_3PO_4 only increase slightly as compared to pure Ag_3PO_4.

Generally, the recombination and separation efficiency of the photogenerated electron-hole pairs has a direct influence on the photocatalytic activity. It is widely known that the recombination of electron-hole pairs can release energy in the form of the fluorescence emission. Therefore, the weaker PL intensity implies the lower electron-hole recombination rate, and results in the higher photocatalytic activity [38]. In Fig. 9a, AP-0 catalyst shows a strong and wide emission peak located between 450 and 490 nm. The doping of SO_4^{2-} into Ag_3PO_4 does not alter the spectral position of the peaks, but successively reduces the overall emission intensity. The weakened emission intensity in AP-3 catalyst means that the energy-wasteful recombination process of electron-hole pairs can be greatly inhibited, which could be a main reason for the superior photodegradation activity of the SO_4^{2-}-doped Ag_3PO_4.

In addition, EIS is a powerful characterization technique to probe the separation efficiency of the electron-hole pairs. Thus the electrochemical properties of pure Ag_3PO_4 and all SO_4^{2-}-Ag_3PO_4 samples were also conducted under visible light irradiation. The typical Nyquist plots of the EIS measurements are shown in Fig. 9b. Generally, the observed semicircle in the EIS Nyquist plot is related
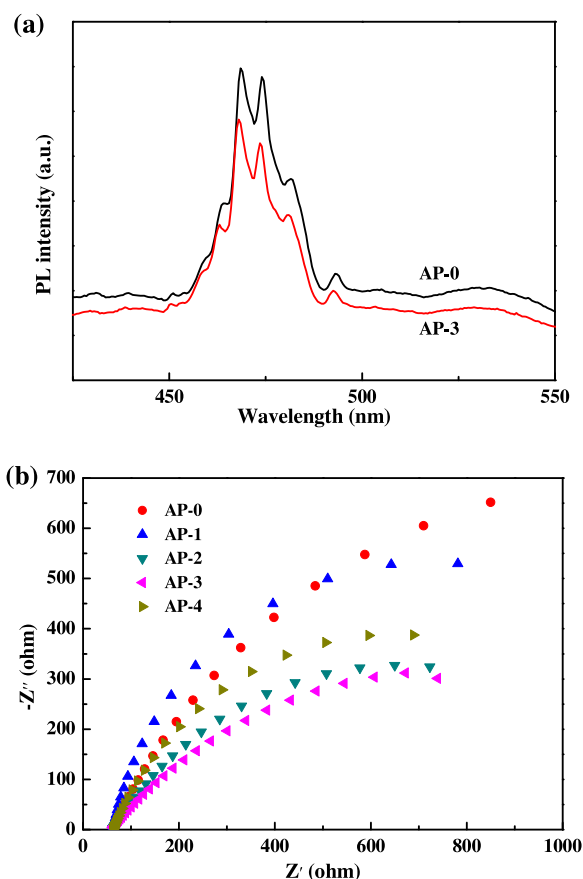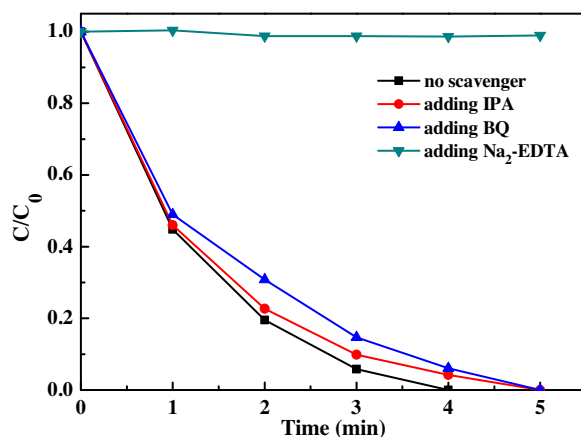
to charge transfer resistance at the catalyst-electrode interface. The smaller radius of the arc corresponds to the higher efficiency of charge transfer process [39]. It is found that the arc radius of SO_4^{2-}-doped Ag_3PO_4 is much smaller than pure Ag_3PO_4. It indicates that doping SO_4^{2-} into Ag_3PO_4 lattice can reduce the charge transfer resistance of Ag_3PO_4 and improve the separation and transfer efficiency of the charges. Noticeably, AP-3 catalyst show the smallest arc, implying the fastest separate efficiency of electron-hole pairs, which is in good accordance with the best photocatalytic performance for RhB and MB photodegradation. As a result, PL and EIS measurements confirm that the higher efficient charge separa-
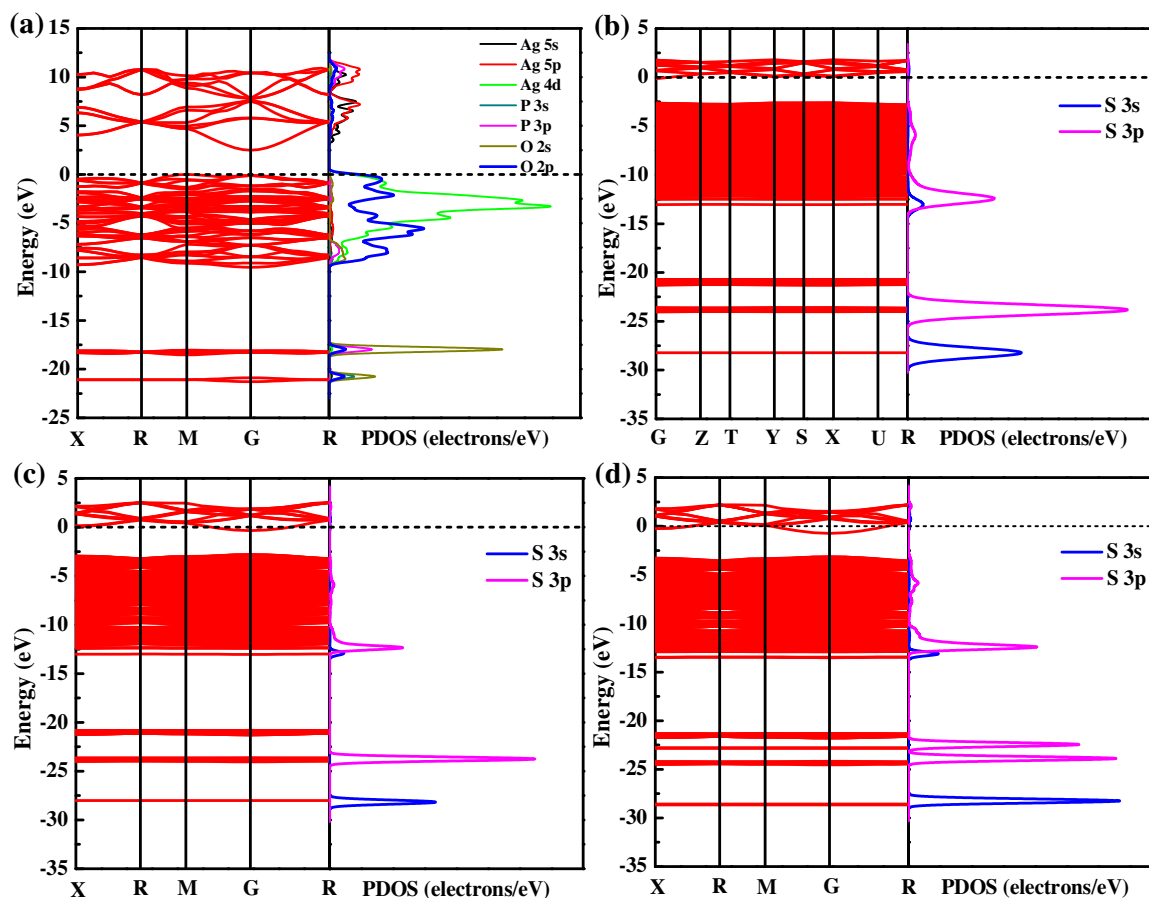
Fig. 11. Band structures and projected density of states (PDOS) for (a) pure Ag_3PO_4, and (b) 2.78 at%, (c) 6.25 at%, (d) 12.5 at% SO_4^{2-}-doped Ag_3PO_4 calculated by the density functional method. The dashed lines in the band structures represent the Fermi level.

tion/transfer of SO_4^{2-}-Ag_3PO_4 is beneficial for the enhancement of the photocatalytic activity.

The reactive species trapping experiments were performed to investigate the predominant reactive oxygen species during the photocatalytic process of SO_4^{2-}-doped Ag_3PO_4. In the experiments, isopropyl alcohol (IPA), p-benzoquinone (BQ) and disodium ethylene diamine tetraacetate (Na_2-EDTA) were separately introduced into the photocatalytic process and acted as the scavengers of hydroxyl radical ($^{\bullet}$OH), superoxide radicals ($^{\bullet}O_2^-$) and photoinduced holes (h^+). Fig. 10 shows the photocatalytic activity of AP-3 catalyst for the photodegradation of RhB in the presence of different scavengers. The addition of IPA and BQ in the RhB solution has no apparent effect on the photocatalytic activity. However, the photocatalytic efficiency is obviously inhibited after the addition of Na_2-EDTA. These results indicate that h^+ serves as the dominant active oxidizing species, while $^{\bullet}$OH and $^{\bullet}O_2^-$ play negligible roles during the photocatalytic process. For pure Ag_3PO_4, the similar results about the reactive species trapping experiments have been also confirmed by previous study [40]. Therefore, the oxidation mechanism of SO_4^{2-}-doped Ag_3PO_4 has not been changed as compared to pure Ag_3PO_4, which is through direct h^+ attack to target organic compounds.

To further elucidate the enhanced photocatalytic performance of SO_4^{2-}-doped Ag_3PO_4, the band structure and density of states of pure Ag_3PO_4 and SO_4^{2-}-doped Ag_3PO_4 with 2.78 at%, 6.25 at%, 12.5 at% dopant concentrations were calculated by the LDA + U method. As shown in Fig. 11a, pure Ag_3PO_4 is an indirect band gap semiconductor. The calculated band gap of pure Ag_3PO_4 is 2.49 eV, which is higher than the experimental value (2.26 eV) due to the well-

known limitation of DFT. Correspondingly, the projected density of states (PDOS) show that the tops of valence bands (VB) are mainly composed of hybridized Ag 4d and O 2p orbitals, and the bottoms of conduction bands (CB) are derived from hybridized Ag 5s, Ag 5p and P 3p orbitals. For SO_4^{2-}-doped Ag_3PO_4, their band gap energies are nearly the same as that of pure Ag_3PO_4. According to the PDOS in Fig. 11b–d, the impurity states generated by SO_4^{2-} doping are mainly distributed in the VB region, and no impurity state appears in the forbidden band gap of SO_4^{2-}-doped Ag_3PO_4. Since S atoms have more valence electrons than P atoms, doping SO_4^{2-} into Ag_3PO_4 lattice can provide extra electrons. As a result, the Femi level of SO_4^{2-}-doped Ag_3PO_4 is significantly shifted towards the conduction band, and SO_4^{2-}-doped Ag_3PO_4 still exhibits n-type character. However, the native defects in pure Ag_3PO_4 acted as "hole killers" cause no intrinsic carries conductivity. The n-type doping in Ag_3PO_4 can enhance carrier concentration and intrinsic conductivity to improve its photocatalytic activity [23].

Meanwhile, the top of VB and the bottom of CB gradually shift towards lower energy regions with increasing dopant concentration. It is noted that the photo-excited holes in the lower energy states have the stronger oxidizability and the photo-generated electrons in the higher energy states possess the more powerful reducibility. Consequently, the oxidative ability of photo-excited holes is enhanced and the reduction potential of photo-generated electrons is suppressed with increasing SO_4^{2-} dopant concentration [41]. During the photocatalytic process, O_2 absorbed on the surface of photocatalysts can be reduced to $^{\bullet}O_2^-$ radicals by the photogenerated electrons, and the surface hydroxyl groups can be trapped by the photogenerated holes to produce $^{\bullet}$OH radi-

cals. The $^\bullet O_2{}^-$, $^\bullet OH$ radicals and holes are strong oxidants in the photocatalytic process. In our radical-trapping experiments, the photooxidation processes occurring on the surface of both $SO_4{}^{2-}$-doped Ag_3PO_4 and pure Ag_3PO_4 are proceeded through direct photo-excited holes, not $^\bullet O_2{}^-$ radicals, to attack target organic compounds. It means that the photogenerated holes for $SO_4{}^{2-}$-doped Ag_3PO_4 play more important roles in the photocatalytic degradation than the electrons. As a result, $SO_4{}^{2-}$-doped Ag_3PO_4 display higher photocatalytic property than pure Ag_3PO_4 in the degradation of organic dyes owing to the enhanced oxidizability.

4. Conclusions

A series of $SO_4{}^{2-}$-doped Ag_3PO_4 catalysts were successfully synthesized by a simple precipitation method. The prepared $SO_4{}^{2-}$-doped Ag_3PO_4 exhibit much higher photocatalytic activities than that of pristine Ag_3PO_4 for the degradation of rhodamine B and methylene blue under visible-light irradiation. The PL and EIS results reveal that the enhanced photocatalytic activity origin from the high separation efficiency of photogenerated electron-hole pairs. The radical trapping experiments show that the photogenerated holes as active oxidizing species play dominant roles in the photocatalytic process. Furthermore, DFT calculations confirm that the conduction bands of $SO_4{}^{2-}$-doped Ag_3PO_4 shift toward the lower energy states, resulting in the stronger oxidizability of photogenerated holes. It further illustrates the expected enhancement of the photocatalytic activity. Thus, this work demonstrates a highly efficient $SO_4{}^{2-}$-doped Ag_3PO_4 photocatalyst via a facile fabrication approach, which may open a new avenue to design the high-performance photocatalysts for future practical applications.

Acknowledgments

References

[1] A. Kudo, Y. Miseki, Chem. Soc. Rev. 38 (2009) 253–278.
[2] H. Tong, S.X. Ouyang, Y.P. Bi, N. Umezawa, M. Oshikiri, J.H. Ye, Adv. Mater. 24 (2012) 229–251.
[3] X.C. Zhang, T.Y. Guo, X.W. Wang, Y.W. Wang, C.M. Fan, H. Zhang, Appl. Catal. B: Environ. 150–151 (2014) 486–495.
[4] H.G. Yang, G. Liu, S.Z. Qiao, C.H. Sun, Y.G. Jin, S.C. Smith, J. Zou, H.M. Cheng, G.Q. Lu, J. Am. Chem. Soc. 131 (2009) 4078–4083.
[5] F. Zuo, K. Bozhilov, R.J. Dillon, L. Wang, P. Smith, X. Zhao, C. Bardeen, P.Y. Feng, Angew. Chem. Int. Ed. 51 (2012) 6223–6226.
[6] G. Miao, L.F. Chen, Z.W. Qi, Eur. J. Inorg. Chem. 35 (2012) 5864–5871.
[7] M. Stucchi, C.L. Bianchi, C. Pirola, S. Vitali, G. Cerrato, S. Morandi, C. Argirusis, G. Sourkouni, P.M. Sakkas, V. Capucci, Appl. Catal. B: Environ. 178 (2015) 124–132.
[8] Z.G. Yi, J.H. Ye, N. Kikugawa, T. Kako, S.X. Ouyang, H.S. Williams, H. Yang, J.Y. Cao, W.J. Luo, Z.S. Li, Y. Liu, R.L. Withers, Nat. Mater. 9 (2010) 559–564.
[9] Y.P. Bi, S.X. Ouyang, N. Umerzawa, J.Y. Cao, J.H. Ye, J. Am. Chem. Soc. 133 (2011) 6490–6492.
[10] B.J. Zheng, X. Wang, C. Liu, K. Tan, Z.X. Xie, L.S. Zheng, J. Mater. Chem. A 1 (2013) 12635–12640.
[11] G.P. Li, Y.X. Wang, L.Q. Mao, RSC Adv. 4 (2014) 53649–53661.
[12] Y.P. Bi, S.X. Ouyang, J.Y. Cao, J.H. Ye, Phys. Chem. Chem. Phys. 13 (2011) 10071–10075.
[13] W.F. Yao, B. Zhang, C.P. Huang, C. Ma, X.L. Song, Q.J. Xu, J. Mater. Chem. 22 (2012) 4050–4055.
[14] L.L. Zhang, H.C. Zhang, H. Huang, Y. Liu, Z.H. Kang, New J. Chem. 36 (2012) 1541–1544.
[15] Q.J. Xiang, D. Lang, T.T. Shen, F. Liu, Appl. Catal. B: Environ. 162 (2015) 196–203.
[16] Y.H. Song, Y.C. Lei, H. Xu, C. Wang, J. Yan, H.Z. Zhao, Y.G. Xu, J.X. Xia, S. Yin, H.M. Li, Dalton Trans. 44 (2015) 3057–3066.
[17] S. Bouhadoun, C. Guillard, F. Dapozze, S. Singh, D. Amans, J. Bouclé, N. Herlin-Boime, Appl. Catal. B: Environ. 174–175 (2015) 367–375.
[18] A.D. Liyanage, S.D. Perera, K. Tan, Y. Chabal, K.J. Balkus, ACS Catal. 4 (2014) 577–584.
[19] M. Luo, Y. Liu, J.C. Hu, H. Liu, J.L. Li, ACS Appl. Mater. Interfaces 4 (2012) 1813–1821.
[20] S.N. Zhang, S.J. Zhang, L.M. Song, Appl. Catal. B: Environ. 152–153 (2014) 129–139.
[21] Y.P. Xie, G.S. Wang, J. Colloid Interface Sci. 430 (2014) 1–5.
[22] H.C. Yu, H.X. Kang, Z.B. Jiao, G.X. Lü, Y.P. Bi, Chin. J. Catal. 36 (2015) 1587–1595.
[23] P. Reunchan, N. Umezawa, J. Phys. Chem. C 119 (2015) 2284–2289.
[24] W.J. Jo, J.W. Jang, K. Kong, H.J. Kang, J.Y. Kim, H. Jun, K.P.S. Parmar, J.S. Lee, Angew. Chem. Int. Ed. 51 (2012) 3147–3151.
[25] H.W. Huang, X.W. Li, J.J. Wang, F. Dong, P.K. Chu, T.R. Zhang, Y.H. Zhang, ACS Catal. 5 (2015) 4094–4103.
[26] H.K. Roobottom, H.D.B. Jenkins, J. Chem. Educ. 76 (1999) 1570–1573.
[27] V.I. Anisimov, J. Zaanen, O.K. Andersen, Phys. Rev. B 44 (1991) 943–954.
[28] B. Mallesham, P. Sudarsanam, G. Raju, B.M. Reddy, Green Chem. 15 (2013) 478–489.
[29] W.R. Cao, L.F. Chen, Z.W. Qi, J. Mol. Catal. A: Chem. 401 (2015) 81–89.
[30] P.Y. Ma, H.J. Yu, Y. Yu, W.M. Wang, H. Wang, J.Y. Zhang, Z.Y. Fu, Phys. Chem. Chem. Phys. 18 (2016) 3638–3643.
[31] D.H. Wang, L. Jia, X.L. Wu, L.Q. Lu, A.W. Xu, Nanoscale 4 (2010) 576–584.
[32] Z. Chen, L.W. Qian, J. Zhu, Y.P. Yuan, X.F. Qian, CrystEngComm 12 (2010) 2100–2106.
[33] M.T. Uddin, Y. Nicolas, C. Olivier, T. Toupance, M.M. Müller, H.J. Kleebe, K. Rachut, J. Ziegler, A. Klein, W. Jaegermann, J. Phys. Chem. C 117 (2013) 22098–22110.
[34] Y.P. Liu, L. Fang, H.D. Lu, Y.W. Li, C.Z. Hu, H.G. Yu, Appl. Catal. B: Environ. 115–116 (2012) 245–252.
[35] J. Cao, B.D. Luo, H.L. Lin, B.Y. Xu, S.F. Chen, J. Hazar. Mater. 217–218 (2012) 107–115.
[36] D. Chen, J.H. Ye, Adv. Funct. Mater. 18 (2008) 1922–1928.
[37] R.S. Mane, W.J. Lee, H.M. Pathan, S.H. Han, J. Phy. Chem. B 109 (2005) 24254–24259.
[38] Y. Park, S.H. Kang, W.Y. Choi, Phys. Chem. Chem. Phys. 13 (2011) 9425–9431.
[39] X.Q. An, J.C. Yu, J.W. Tang, J. Mater. Chem. A 2 (2014) 1000–1005.
[40] T.J. Yan, H.W. Zhang, Y.P. Liu, W.F. Guan, J.L. Long, W.J. Li, J.M. You, RSC Adv. 4 (2014) 37220–37230.
[41] J.G. Yu, P. Zhou, Q. Li, Phys. Chem. Chem. Phys. 15 (2013) 12040–12047.